Journal of
Materials Chemistry C

ROYAL SOCIETY
OF CHEMISTRY

PAPER

View Article Online
View Journal | View Issue

Check for updates

Cite this: *J. Mater. Chem. C*, 2022, **10**, 12032

Understanding the structure-band gap relationship in $SrZrS_3$ at elevated temperatures: a detailed *NPT* MD study†

Namrata Jaykhedkar,[ab] Roman Bystrický,[ac] Milan Sýkora*[a] and
Tomáš Bučko *[bc]

Thermal effects on the structure, bulk modulus (B_0), and electronic band gap (E_g) of the needle-like (NL) (NH_4CdCl_3 structure type) and distorted perovskite (DP) ($GdFeO_3$ structure type) phases of $SrZrS_3$ were investigated over the temperature range 300–1200 K by means of *ab initio* molecular dynamics in an *NPT* ensemble, accelerated by adaptive machine learning. An anisotropic thermal expansion of a distinctly different quality was observed for the two phases. While all lattice vectors of the NL phase expand monotonously with *T*, the thermal behavior of the DP phase is more complex, with two vectors (**b** and **c**) monotonously expanding and one (**a**) contracting after an initial expansion. We show that the thermally-induced structural changes in the DP phase are a consequence of proximity of the cubic phase (C), into which it transforms quasi-continuously upon heating. A linear decrease of B_0 with *T* (from 45.9 GPa to 33.6 GPa for NL and from 66.8 GPa to 48.5 GPa for DP) is predicted. Since the temperature dependent E_g values are determined as the *NPT* ensemble averages, both the lattice expansion and the electron–phonon coupling effects are naturally taken into account in our simulations. We found that the E_g for NL is nearly constant, while that for DP decreases by as much as ~0.5 eV within the studied temperature range. The latter is shown to be almost exclusively due to a very large atomic displacement contribution resulting from the proximity of the parent C phase, with the E_g ~ 0.8 eV lower than that of the DP phase.

Received 30th May 2022,
Accepted 7th July 2022

DOI: 10.1039/d2tc02253b

rsc.li/materials-c

1 Introduction

Over the past decade, there has been a great deal of interest in the materials from the Hybrid Organic–Inorganic Perovskites (HOIPs) family due to their favourable properties for the use in photovoltaics and other optoelectronic applications.[1–7] Although the HOIPs show a great potential, their broader commercial exploitation has so far been hindered by a limited thermal and chemical stability and a toxicity associated with the presence of lead in their structure.[8,9] Recently, it has been proposed that ternary chalcogenides (TCs) with the general formula ABX_3 (where A and B are metals and X is S or Se), especially with the perovskite crystal structure, may be an appealing alternative, thanks to the electronic properties analogous to HOIPs, and a broad variety of possible chemical compositions that can be chosen to avoid the use of lead or other toxic metals.[10–12] It has also been shown that the experimentally prepared TCs exhibit good chemical properties and a high thermal stability.[9,13–16]

From the perspective of practical applications of TCs in optoelectronics, it is important to understand how they are affected by various thermodynamic conditions. In this regard, previous studies focused mainly on the pressure dependence of the band gap (E_g). In their experimental work, Gross *et al.*[17] found that E_g of $BaZrS_3$ decreases with pressure, at the average rate of ~ -0.015 eV GPa^{-1}, over the 0 to 8.9 GPa range. A modest monotonous decrease of E_g with pressure was reported for several TCs in recent theoretical studies.[18,19] One of the prerequirements for effective exploitation of new materials in applications is an understanding of how their electronic properties vary with temperature. In many materials, variations in temperature over a practically relevant range can induce structural distortions and even phase transitions which may cause significant and abrupt changes in the material's physical and electronic properties, such as lattice parameters, electronic band gap, electrical conductivity and many others. An understanding of the temperature dependent behavior is also

---

[a] *Laboratory for Advanced Materials, Faculty of Natural Sciences, Comenius University, Ilkovičova 6, 842 15 Bratislava, Slovakia. E-mail: sykoram@uniba.sk*
[b] *Department of Physical and Theoretical Chemistry, Faculty of Natural Sciences, Comenius University in Bratislava, Ilkovičova 6, 842 15 Bratislava, Slovakia. E-mail: tomas.bucko@uniba.sk*
[c] *Institute of Inorganic Chemistry, Slovak Academy of Sciences, Dúbravská Cesta 9, 845 36, Bratislava, Slovakia*

† Electronic supplementary information (ESI) available. See DOI: **https://doi.org/10.1039/d2tc02253b**

important for identifying appropriate experimental conditions for preparation of materials with desired electronic properties. While temperature dependent effects have been observed and systematically studied in ternary halogenides and oxides, such as $CsPbBr_3$,[20] $CH_3NH_3PbI_3$,[21] $CH_3NH_3PbBr_3$,[20] or $SrTiO_3$,[22] similar studies have been lacking in case of TCs.

In this work, our goal is to partially address this deficiency by performing a theoretical investigation of the finite temperature properties (including the band gap) of a representative TC material, $SrZrS_3$. Our choice of the material is motivated by the fact that $SrZrS_3$ is one of the few TCs that have been experimentally prepared in two crystal phases, both stable at ambient conditions:[13,15,23–26] type NH_4CdCl_3 (also known as needle-like (NL) phase) and type $GdFeO_3$ (also known as distorted perovskite (DP) phase). At ambient conditions the two phases differ substantially in their E_g (1.53 eV (NL) *vs.* 2.13 (DP))[15,23] and absorption properties. In their theoretical study of 18 TCs, Sun *et al.*[23] have shown that the materials in the DP phase have better absorption properties than the NL phase. It has been suggested in experimental work of Niu *et al.*[15] that although the band gaps of $BaZrS_3$ or $SrZrS_3$ in DP phase are suboptimal, their excellent optical properties still qualify them as suitable candidates for solar cell materials and a similar conclusion was made also in a recent experimental and theoretical work of Nishigaki *et al.*[27] Here we systematically investigate temperature-induced changes in the structure of both phases in the temperature range of 300–1200 K, and the effect of these structural changes on the electronic structure, particularly E_g. We find that, while the structural and electronic changes are relatively small for the NL phase, they are quite substantial for the DP phase, with the band gap shifting closer to the optimal photovoltaic range when temperature is increased. Based on our analysis, we expect similar effects to be observed also for other TCs. Our results indicate that more systematic investigations and screening of temperature dependent properties of TCs are likely to provide important insights in the search for the most promising candidate materials for photovoltaics and other optoelectronics applications.

The most popular approach to study E_g dependence on T by *ab initio* computer simulations is the Allen–Heine–Cardona (AHC) method,[28,29] successfully applied to the pristine and the oxygen-vacant cubic $LaCrO_{3-\delta}$,[30] $CH_3NH_3PbI_3$,[31] or $SrTiO_3$[22] and other materials. The AHC method, however, suffers from several important limitations, such as the neglect of lattice thermal expansion contribution, or the use of rigid ion approximation in calculating the one-electron eigenvalues associated with the atomic displacement. The latter problem can be eliminated by Monte Carlo sampling of the quantum harmonic oscillations, which can be realized also as a 'one-shot' calculation, if a sufficiently large supercell is used, as recently proposed by Zacharias and Giustino.[32] As shown by Karsai *et al.*,[33] this method can be combined with the quasi-harmonic approximation[34] (QHA) to account also for the lattice thermal expansion, which was found to be crucial for accurate predictions of the temperature dependence of E_g for diamond. Unfortunately, the QHA is not reliable for materials with highly anharmonic modes, especially if high temperature properties are of interest. An uncompromising solution to this problem is the use of molecular dynamics in an *NPT* ensemble (*NPT* MD), which allows a consistent treatment of lattice thermal expansion and electron–phonon effects within one simulation protocol. Until recently, the computational time needed to obtain well converged results from *NPT* MD was impractically large compared to the more approximate approaches such as QHA. With the recent development of the machine learning force field (MLFF), implemented in VASP 6.3,[35,36] however, ab initio-quality *NPT* MD became feasible for routine applications, with the CPU cost comparable to the QHA. Among the advantages of this method is that the training configurations are chosen automatically and on-the-fly during a training *ab initio* MD run based on the similarity with other training configurations and the quality of predictions of energies, forces, and stress tensor components. A well-trained MLFF provides *ab initio* quality results at a fraction of time of an explicit *ab initio* calculation, enabling thus improvements in sampling quality *via* performing longer MD simulations. The MLFF approach can be used to study many important physical properties including the entropy-driven hcp–bcc phase transition of zirconia,[37] the heat transport properties of ZrO_2 at ambient pressure,[38] or the hydration free energies of oxygen atoms and hydroxyl groups adsorbed on the Pt surfaces in water.[39] Inspired by a successful use of this approach in the investigation of temperature-stimulated phase transitions of hybrid perovskite materials $MAPbI_3$ and $CsPbI_3$,[40] we employ it here to explore thermal effects on the structure and band gap of the NL and DP phases of a prominent TC material $SrZrS_3$.

This paper is organized as follows: the methodology used in this work is described in Section 2, reference zero-temperature results are discussed in Section 3.1, thermal effects on the structure and electronic band gap are analyzed in Sections 3.2 and 3.3, respectively, and summary of the most important results is provided in Section 4.

2 Methods and materials

2.1 Computational methods

The calculations were performed using the periodic density-functional theory (DFT) code Vienna Ab-initio Simulation Package (VASP).[35,36] The Kohn-Sham equations were solved variationally in a plane-wave basis set with the maximal kinetic energy of 400 eV using the projector-augmented-wave (PAW) method of Blöchl,[41] as adapted by Kresse and Joubert.[42] Unless stated otherwise, the Perdew, Burke, and Ernzerhof (PBE) exchange–correlation functional in the generalized gradient approximation proposed by Perdew *et al.*[43] was used. The convergence criterion for the electronic self-consistency cycle, measured by the change in the total energy between successive iterations, was set to 10^{-6} eV per cell.

Just like other perovskites, $SrZrS_3$ forms lower symmetry variants of its parent cubic phase at the ambient conditions. The low temperature NL phase transforms into the DP phase at $\sim$1250 K.[13] Although the NL phase is thermodynamically stable

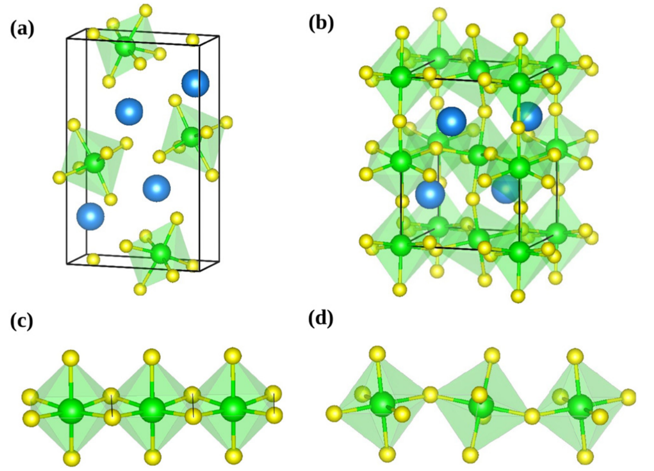

Fig. 1 Conventional unit cell of needle like (a) and distorted perovskite (b) phases of $SrZrS_3$. The needle like structure forms one-dimensional chains of ZrS_6 octahedra connected *via* edge-sharing (c), while the distorted perovskite form comprises a three-dimensional network of corner-sharing ZrS_6 octahedra (d). The blue, green and yellow colored spheres represent the Sr, Zr and S atoms respectively.

at room temperature, the DP structure can also be prepared as a long-lived metastable phase. Both types of crystals are orthorhombic, belonging to the *Pnma* space group. The experimentally determined geometries of conventional unit cells (Fig. 1) are compiled in Table 1. The optimizations of NL and DP structures were carried out for conventional unit cells using an external optimizer Gadget.[44] In the relaxed structures, all forces acting on the atoms were below 5×10^{-3} eV Å^{-1}. The grids of $4 \times 8 \times 2$ and $4 \times 4 \times 4$ *k*-points were used to sample the Brillouin zone for relaxations of NL and DP, respectively.

Molecular dynamics (MD) simulations were performed in an *NPT* ensemble at zero pressure and temperatures of 300 K, 600 K, 900 K, 1200 K and 1500 K. The simulation temperature was controlled by Langevin thermostat with a friction coefficient of 2 ps^{-1} for all atoms. The pressure was controlled by a Parrinello–Rahman barostat,[45,46] whereby a mass of 2 amu and a friction coefficient of 10 ps^{-1} were used for the lattice degrees of freedom. The equations of motion of the ions were integrated using the velocity Verlet algorithm,[47] with a time step of 3 fs. Supercells consisting of $2 \times 4 \times 1$ and $2 \times 2 \times 2$ multiples of conventional unit cells (both containing 160 atoms) were used in the MD simulations of NL and DP phases, respectively. This choice was made to account for the most essential atomic motions and to keep the crystal structures close to the cubic shape, allowing the use of the same computational settings in all simulations. As demonstrated in Section SII (ESI†), further increase in the size of the supercells does not lead to significant variations in the lattice parameters or radial distribution functions of the predicted structures. Consistently with the setting used in relaxations, the *k*-points grid was set to $2 \times 2 \times 2$ in all MD simulations.

Table 1 Comparison of optimized lengths of lattice vectors (*a*, *b*, *c*), volumes (*V*) of conventional unit cells, and bulk moduli (B_0) of needle like (NL), distorted perovskite (DP), and cubic (C) phases of $SrZrS_3$ obtained from static calculations with available experimental and theoretical data. The values in the parentheses correspond to the cubic cell expressed in the setting of distorted perovskite structure (*cf.* Fig. 2)

	a (Å)	*b* (Å)	*c* (Å)	*V* (Å^3)	B_0 (GPa)
NL phase					
Exp.[13]	8.525	3.826	13.925	454.1	—
Exp.[15]	8.504	3.820	13.917	452.1	—
DFT (this work)	8.649	3.840	14.015	465.4	50.3
DP phase					
Exp.[13]	7.108	9.772	6.741	468.2	—
Exp.[16]	7.103	9.758	6.731	466.5	—
DFT (ref. 18)	7.147	9.843	6.804	478.7	
DFT (this work)	7.169	9.829	6.787	478.2	69.7
C phase					
DFT (ref. 18)	5.016			126.2	73.5
DFT (this work)	5.007 (7.082)	(10.015)	(7.082)	125.6 (502.3)	73.3

To accelerate our computationally demanding MD simulations, the machine learned force field (MLFF) recently implemented in VASP 6.3[35,36] was employed. The MLFF uses descriptors based on Gaussian representation of atomic distribution[36,48] and predicts the target properties – energies, forces and stress tensor components – *via* Bayesian linear regression. Consequently, the quality of predictions can be measured by Bayesian error estimator.[35,49] Importantly, the training configurations are chosen automatically and on-the-fly during an MD run, based on the similarity with other training configurations. This strategy ensures that new training configurations are added whenever an unexplored part of the configuration space is visited. In our calculations, a separate training procedure for each phase and temperature was executed with the initial Bayesian error threshold of 0.01 eV Å^{-1}. The training typically consisted of 2×10^4 MD steps but the actual number of DFT calculations was much lower (150 to 600, depending on the temperature) and hence the training procedure was relatively fast. Once the training procedure was completed, a production run of length of ∼3 ns was performed at the MLFF level and the corresponding data were used to determine the observables. The use of MLFF allowed for enormous CPU time savings compared to a direct DFT (time needed to complete one MD step decreased from 1.6 CPU-hours to only 0.069 CPU-hours) while maintaining the *ab initio* quality of simulations, as discussed in more detail in Section SI (ESI†).

Upon performing the MD simulations, the equilibration period was determined using statistical Mann–Kendall tests,[50] applied to averages and variances of all measured quantities. Upon discarding the data corresponding to the equilibration period, the remaining data (production period) exhibited no statistically significant trend and were used to calculate the ensemble averages. The standard error for computed properties was determined using the blocking method.[51] The statistical uncertainty was predicted by assuming the confidence interval of 95% (*i.e.*, the quantile of 1.96 was used). The basic observables such as the structural parameters or band gap values were computed as simple averages over the *NPT* ensemble. Linear and volume expansion coefficients were calculated *via*

$$\alpha_X = \frac{1}{\langle X \rangle_{T_{\text{ref}}}} \left(\frac{\mathrm{d}\langle X \rangle}{\mathrm{d}T} \right)_{p,T}, \tag{1}$$

where $\langle\cdots\rangle$ stands for an ensemble average of cell volume or length of a cell vector (X), T_{ref} is set to 300 K and the differentiation was performed analytically on a third order polynomial fit of the $\langle X\rangle$ *vs.* T dependence. The isothermal bulk modulus (B_0) was computed using finite differences approximation to defining formula:

$$B_0 = -V\left(\frac{\partial p}{\partial V}\right)_T \approx -\left(\frac{V(T,\Delta p) - V(T,-\Delta p)}{2V(T,0)\Delta p}\right)^{-1}, \qquad (2)$$

where the volumes V (X, Y) represent the *NPT* ensemble averages determined for $T = X$ and $p = Y$. A step of $\Delta p = 0.5$ GPa was used in the numerical differentiation in eqn (2).

Drawings of structures presented in this work were created using the program VESTA.[52]

2.2 Experimental methods

2.2.1 Materials. The DP form of $SrZrS_3$ was prepared by reaction of $SrZrO_3$ with sulfur in the presence of small amount of boron. For the synthesis, the reaction mixture was ground in the agate mortar and loaded into a quartz tube with the inner diameter of 15 mm. The tube was evacuated to 2 Pa and flame sealed. The sample was placed in a tube furnace and heated at 1270 K for 36 hours.

2.2.2 XRD measurements. High temperature XRD measurements were performed on Panalytical Empyrean diffractometer coupled with Anton Paar high-temperature chamber HTK-16 N using Pt heating strip in air and in the N_2 atmosphere. The heating rate during non-isothermal segments was 8 K min^{-1}. The duration of the isothermal segments during which the patterns were collected was 90 s. The temperature step for collecting the individual patterns was 20 K. Rietveld analysis for lattice parameters determination was done using HighScore plus on scans with 2θ ranging from 15° to 55° with a step of 0.026°.

3 Results and discussion

3.1 Static calculations

Before discussing the finite-temperature properties of $SrZrS_3$ (*vide infra*), it is useful to explore the structure, energetics, elastic and electronic properties of this material by means of static calculations. Since the results presented here correspond to a classical zero temperature thermodynamic limit, they will serve as a reference for the discussion of finite-T properties.

The energy *versus* volume dependence was obtained in a series of constant volume relaxations performed for each phase, which was subsequently fitted to Murnaghan equation of state[53] to determine the ground state volume and bulk modulus. The ground state geometry was then obtained in a relaxation with the cell volume fixed at the ground state value. Finally, the band structure calculation was performed for the relaxed ground state structure.

The computed ground state quantities are compiled in Table 1. As it can be seen from the presented data, the relative errors with respect to the experimental values[13,15] are within 1.7% for the lattice constants and within 2.9% for the cell volume.

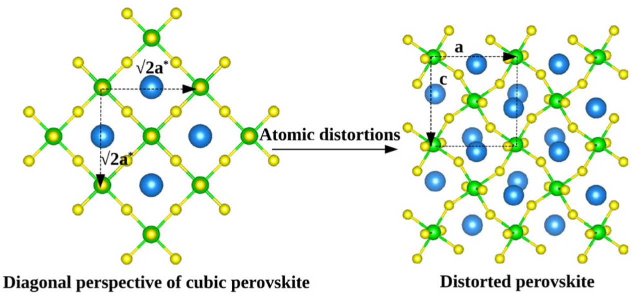

Fig. 2 Schematic graphical representation of the formation of the distorted perovskite (DP) from a more symmetric cubic (C) phase of $SrZrS_3$. The conventional lattice vectors of the C phase are transformed in the setting of the phase DP as follows: $\mathbf{a} = \sqrt{2}\mathbf{a}_1^*$, $\mathbf{b} = 2\mathbf{a}_2^*$, $\mathbf{c} = \sqrt{2}\mathbf{a}_3^*$, with $\mathbf{a}_i^*$ being the i-th lattice vector of the undistorted cubic cell. The blue, green and yellow coloured spheres represent the Sr, Zr and S atoms respectively.

We notice, however, that our calculations systematically overestimate the structural parameters. Since the experimental measurements were conducted at a finite temperature (298 K for both the NL and DP phases), it can be expected that the actual relative error should increase further when the finite temperature effects are taken into account. We hypothesize that this small systematic overestimation of the lattice parameters is due to an incorrect treatment of long-range London dispersion interactions, which is a well-known shortcoming of (semi-)local density function approximations.[54] Although several different correction schemes are currently available to alleviate this problem,[55–61] a dedicated theoretical study would be necessary to identify the method that works best for the system at hand. We emphasize, however, that the systematic error remains very small (within 2%) even when the thermal effects are taken into account, as we discuss in Section 3.2. Hence, the choice of the simulation method in this study is justified.

Although the energies of the ground state structures of the NL and DP phases are very similar, the former is slightly more stable at 0 K with the energy difference being only 2 meV $\mathrm{f.u.}^{-1}$. The lower ground state energy of the NL phase is consistent with the experimental observation that this phase is stable at the temperatures below 1250 K, while DP is thermodynamically preferred at higher T.[13]

The computed values of the bulk modulus suggest that the NL phase is more compressible than the DP phase. This is a direct consequence of the atomic arrangement in the NL phase, which lacks the rigid three dimensional covalent network of octahedra, present in the DP phase (Fig. 1).

As it will be discussed in more detail in Section 3.2, it is crucial for understanding of the thermal behavior of the DP phase that its structure has its origin in the undistorted cubic (C) phase. The transformation is a result of symmetry lowering distortions (thus the name 'distorted perovskite'), as shown schematically in Fig. 2. Thus, one can represent the C phase in the setting of DP by choosing the lattice vectors of the former as follows: $\mathbf{a} = \sqrt{2}\mathbf{a}_1^*$, $\mathbf{b} = 2\mathbf{a}_2^*$, and $\mathbf{c} = \sqrt{2}\mathbf{a}_3^*$, where $\mathbf{a}_i^*$ represents a lattice vector of a primitive cell of C. By comparing the cell geometries of the DP and C phases given in Table 1 one can see that, due to the distortions, the values of **c** and **b** are shortened by 4.2% and 1.9% respectively while **a** is elongated by 1.1% and the cell volume is reduced by 4.8%. In terms of energy, the symmetry breaking of the cubic structure into the DP phase results in stabilization by as much as 705 meV f.u.$^{-1}$. Counter-intuitively, the C phase with lower density is predicted to be slightly less compressible than the more condensed DP phase, as evident from the computed values of bulk modulus (B_0) shown in Table 1. Importantly, vibrational analysis of the unperturbed cubic phase reveals that the C phase is unstable at low T, as indicated by the presence of several vibrational modes with imaginary frequencies in the center of Brillouin zone (see Table S4 (ESI†)). Consistently with this conclusion, there are currently no experimental reports of the preparation of the $SrZrS_3$ in the cubic phase.

The three phases of $SrZrS_3$ discussed here exhibit distinctly different band gaps (E_g). Using the PBE functional, we predict the values of 0.61 eV, 1.23 eV and 0.47 eV for NL, DP, and C respectively. We note that the the band gap of NL and DP is direct,[18,23] at the Γ point of the Brillouin zone (BZ), while that of C is indirect (see Fig. S7 and S8 (ESI†)).[18] The latter emerges as a difference between the conduction band value in the center (Γ point) and valence band at the edge (point R) of BZ defined for the primitive cell of C. Therefore, the zone folding[62,63] due to the use of the DP setting for the C lattice remaps the maximum of the valence band onto the Γ point (Fig. S8 (ESI†)) and the band gap becomes direct. It is evident from the comparison with the available experimental data[15] that the PBE functional underestimates the measured values ((1.53 eV (NL), 2.05–2.13 eV (DP))) by $\sim$0.9 eV for both phases. As reported previously,[23] this error can be significantly reduced by using the HSE06 functional.[64–66] Indeed, the band gaps computed at the HSE06 level (1.40 eV (NL), 2.04 eV (DP) and 1.21 eV (C)) are in a reasonable agreement with the experimental reference. We also note that the PBE and HSE06 results obtained in this work are in a very good agreement with previous theoretical reports.[18,23] Finally, we remark that we neglected the thermal effects in the simulations presented so far – as we shall show in Section 3.3, these are small at T = 300 K, the temperature at which the experimental measurements were conducted.[15]

3.2 Thermal effects on crystal structure

In order to study the finite temperature effects on the structure of $SrZrS_3$, *ab initio NPT* MD simulations accelerated by MLFF[35,36] were performed, as described in Section 2.1. To this end, two series of independent MD runs, one initialized from the NL and the other from the DP structure, were executed for the temperatures of 300 K, 600 K, 900 K, 1200 K, and 1500 K (only DP). The simulation settings related to the electronic structure calculations used to train the MLFF were consistent with those used in the static calculations discussed in Section 3.1.

The finite temperature values of structural parameters for the NL and DP phases are listed in Table 2. Plots with the thermal variations of parameters are shown in Fig. S3 and S4 (ESI†). As can be seen from the data, our calculations overestimate somewhat the cell sizes at room temperature. The overestimation is approximately isotropic and similar in magnitude for both stable phases. Nevertheless, the agreement with the experiment is reasonable (within 2.0% for the lengths of lattice vectors and within 4.3% for the cell volumes).

Table 2 Lengths of lattice vectors (*a*, *b*, *c*), and volumes (*V*) of conventional cells, and isothermal bulk moduli (B_0) determined using *NPT* MD for the needle like (NL), distorted perovskite (DP) and (pseudo-) cubic (C) phases of $SrZrS_3$ at various temperatures. The values in the parentheses correspond to the cubic cell expressed in the setting of the DP structure (see Fig. 2). The 0 K results correspond to the relaxed structures

T (K)	a (Å)	b (Å)	c (Å)	V (Å^3)	B_0 (GPa)
NL phase					
0	8.649	3.840	14.015	465.4	50.3
300	8.674	3.858	14.098	471.7	45.9
600	8.713	3.878	14.185	479.3	42.1
900	8.758	3.901	14.277	487.7	37.8
1200	8.815	3.926	14.372	497.2	33.6
DP phase					
0	7.169	9.829	6.787	478.2	69.7
300	7.177	9.868	6.827	483.5	66.8
600	7.182	9.915	6.876	489.7	60.4
900	7.182	9.973	6.936	496.7	54.3
1200	7.150	10.037	7.033	504.5	48.5
(Pseudo-)C phase					
0	5.007 (7.082)	(10.015	(7.082))	125.6 (502.3)	73.3
1200	5.017 (7.099)	(10.031)	(7.098)	126.3 (505.2)	48.5
1500	5.505 (7.142)	(10.103)	(7.143)	128.8 (515.2)	42.9

Across the temperature range examined here, the thermal effects cause smooth but anisotropic expansion of the NL and DP lattices. We note that NL is known to transform to DP at 1250 K.[13] However, this first order phase transition is associated with re-connection of covalent Zr–S bonds, which is an activated process that, due to the time scale problem, can not be effectively studied by straightforward MD simulations used here. As shown in Fig. 3, the lattices of both phases differ in their thermal behavior. In NL, the linear thermal expansion coefficients for all three lattice vectors increase monotonously with T and eventually converge to approximately the same value at 1200 K (Fig. 3), *i.e.*, the lattice expansion becomes virtually isotropic at this point. In the DP, in contrast, the differences in α increase with T, whereby the coefficient for the lattice vector a monotonously decreases and even becomes negative at $T > 750$ K. Hence, although the coefficients α_b and α_c are significantly larger at $T > 500$ K in the case of DP than in the case of NL, the volume expansion of the NL lattice is actually larger over the entire temperature range examined here (Fig. 3).

The key observation to explain the behavior of DP is that it converts quasi-continuously into undistorted cubic structure upon heating: the lattice parameters a and c become identical while the lattice constant b approaches the value of $a/\sqrt{2}$. This interpretation is also supported by the results of our in-house temperature-dependent X-ray diffraction measurements (Fig. 4) although a high enough temperature needed to observe the cubic phase was, due to the sample oxidation, not reached. As demonstrated earlier, the deformation of the unperturbed cubic structure yielding the DP phase involves a significant shortening of c (4%), a relatively small contraction along b

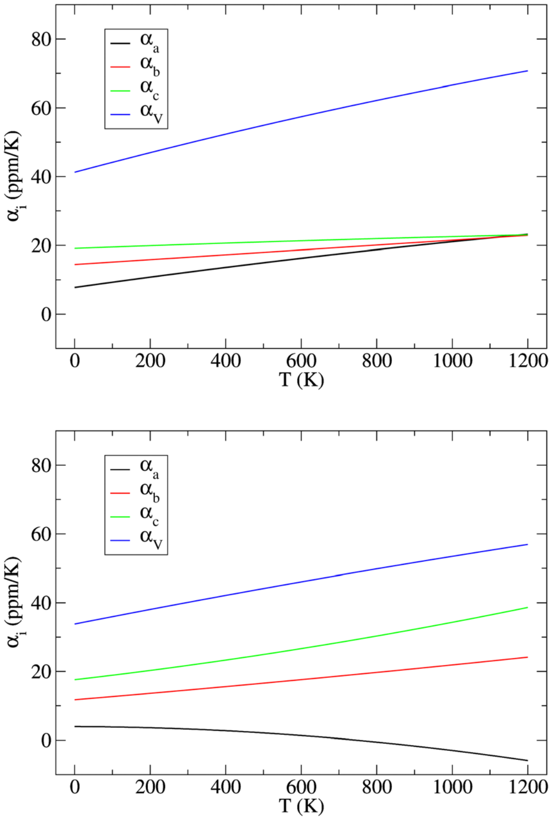

Fig. 3 Variation of linear (α_a, α_b, and α_c) and isotropic (α_V) thermal expansion coefficients in the NL (top) and DP (bottom) phases of $SrZrS_3$ with temperature.

(2.3%) but a slight expansion of *a* (1.5%). The reverse structural changes occur at high temperatures when the DP phase is transformed into the (pseudo-) C phase. Hence, the observed changes in the expansion coefficients, especially at high temperatures, are a direct consequence of the formation of the cubic phase.

At T = 1200 K, the cell volume of DP phase is only slightly larger than that of the relaxed structure of the phase C (Table 2). Also the kinetic energy $\left(\frac{3}{2}Nk_BT \approx 0.748 \text{ eV f.u.}^{-1}\right)$ is now higher than the potential energy difference between the relaxed C and DP structures (0.705 eV f.u.^{-1}), making the DP to C transition feasible. By monitoring the values of lattice parameters *a* and *c* (see Fig. S9 (ESI†)), multiple abrupt switching events between the DP and C phases are observed, suggesting that both phases are close to coexistence (although the C phase already prevails). Hence, although temperature increase facilitates a seemingly gradual conversion from DP to C, the phase transition is still of the first order. The DP to C transformation is virtually complete at 1500 K as is evident from the values of lattice constants in Table 2 and inspection of the atomic positions and lattice parameters averaged over all MD-generated configurations (Fig. S10 (ESI†)).

A useful insight into the temperature-induced changes in internal structure can be gained from an analysis of partial radial distribution functions (RDF) for the Zr–S pairs (Fig. 5).

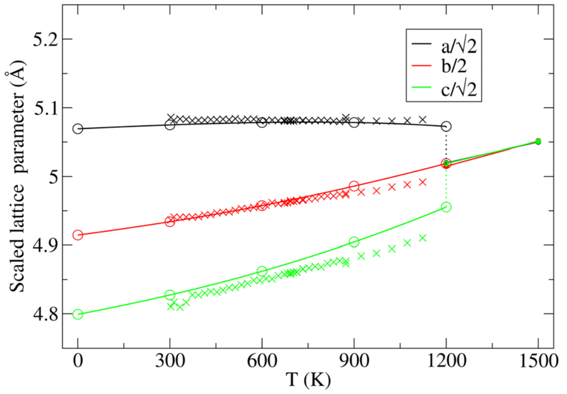

Fig. 4 Variation in the average lengths of scaled lattice vectors $\mathbf{a}/\sqrt{2}$, $\mathbf{b}/2$, and $\mathbf{c}/\sqrt{2}$ of DP/C phase of $SrZrS_3$ with temperature. Circle and cross symbols represent the theoretical and experimental results, respectively. To facilitate a clearer comparison with theory, which tends to slightly overestimate the lengths of the lattice vectors (see. Table 1), all experimental data points were shifted by a constant value of 0.05 Å. Note that, according to the theoretical predictions, DP and C coexist at 1200 K. At T = 1500 K, conversion of DP to C is complete and therefore all three values of scaled lattice parameters coincide.

The positions of the first peaks on the RDF, corresponding to the nearest neighbor distance, are 2.59 Å (NL) and 2.56 Å (DP), which are to be compared with the experimentally reported average bond lengths of 2.57 Å (NL) and 2.55 Å (DP).[13] Regardless of the $SrZrS_3$ phase, the position of this RDF peak gradually shifts to smaller values with increase in T, reaching the value of 2.53 Å at 1200 K. The RDFs evaluated separately for the DP and the C phases at 1200 K are virtually identical (see Fig. S11 (ESI†)), indicating that the local structure of both phases is very similar at these conditions. The latter is also the reason why multiple phase transitions have been observed within our MD run (*vide supra*). Also, this result shows that the internal structure is not yet fully transformed into the C phase (*cf.* RDF for 1500 K), as one could incorrectly assume based on the lattice geometry (Table 2). The gradual shift of the peak maximum towards lower values (2.51 Å) continues all the way to 1500 K, where the C phase formation is virtually complete.

The likelihood of a temporary Zr–S bond breaking increases with T, which is evident from the increase in the RDF amplitude in the region $r \leq 3.0$ Å. This effect is more pronounced in the NL than in the DP/C (at 1200 K, for instance, the RDF amplitude at r = 3.0 Å reaches the values of 0.75 and 0.55 for the NL and the DP/C, respectively). As mentioned above, the Zr–S re-connection is a prerequisite for the NL to DP phase transition to take place. Hence, although the phase transition did not spontaneously occur within our simulations, the increased likelihood of the Zr–S bonds breaking can be viewed as a sign of proximity to such a process.

In the case of the NL, a gradual disappearance of the RDF peak at $r \approx 5.2$ Å, representing the inter-chain non-bonding Zr–S distance, is observed. This is caused by a temperature induced deformation of the chain of edge-sharing octahedra (see Fig. S12 (ESI†)). In the case of the RDF evaluated for simulations initialized from the DP phase, a gradual transition

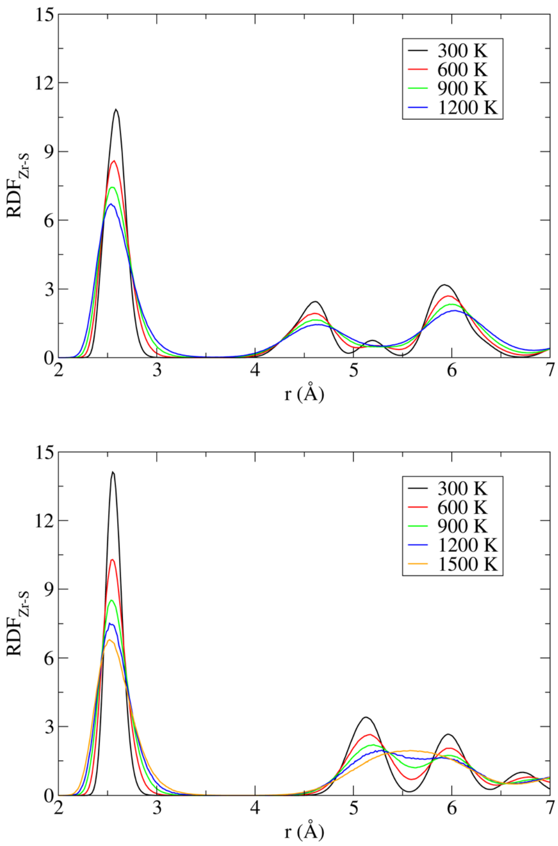

Fig. 5 Radial distribution function for the Zr–S pairs (RDF$_{Zr-S}$) in the NL (top) and DP/C (bottom) phases of $SrZrS_3$ at various temperatures.

from the DP to the C phase is observed, which is evident from the reduction of separation between the two initially well-resolved next-nearest neighbour peaks located at $r \approx 5.1$ Å and $\sim$6.0 Å that are being progressively replaced by one broad band centered at $r \approx 5.6$ Å representing the next-nearest Zr–S distance in a perfect cubic structure.

The values of the isothermal bulk modulus, determined as described in Section 2.1, are presented in Table 2. The results indicate that the NL phase is less compressible than the DP phase at all temperatures considered, whereby the difference in the B_0 is 15–21 GPa. As expected, bulk modulus decreases approximately linearly with T and the DP to C phase transition seem to have only a modest effect on the B_0 *vs.* T dependence.

3.3 Thermal effects on electronic band gaps

The results and conclusions reached in the previous section motivate an important question: How do the temperature-induced structural changes affect the electronic properties of $SrZrS_3$? To address this question, electronic band gap values for all relevant phases were calculated as ensemble averages at each temperature. For this purpose, we made use of the configurations generated in long MD runs used to analyze the T-dependent structure (see Section 3.2) out of which we randomly selected a representative set of 200 configurations. For each of the selected configurations, a single point electronic structure calculation has been performed at the DFT level. Finally, the band gap observables for each T were obtained as arithmetic averages over the representative set members. As discussed in Section 3.1, the NL and DP phases have a direct band gap at the Γ point of the BZ while the indirect band gap found in C appears as a direct gap at Γ when the DP setting is used in calculations (Fig. S8 (ESI†)). Since the integral multiples of conventional NL and DP cells were used in our MD calculations, we were able to determine the band gap conveniently as a difference between the Γ point values of the lowest conduction and highest valence bands. The E_g distributions determined for each T are shown in Fig. S13 (ESI†). The resulting averages of E_g exhibit a very small statistical uncertainty (within 0.002 eV).

The resulting T-dependences of the band gaps of NL, DP and C phases are shown in Fig. 6. The NL and DP phases exhibit a distinctly different behavior: while E_g of the former is virtually constant over the entire temperature range (no finite T value deviates from the zero T value by more than 0.05 eV), the band gap of the latter monotonously and steeply decreases with T, whereby the difference between the values determined for 1200 K and 0 K is as large as 0.45 eV. The values of E_g computed for DP and C at 1200 K, at which both phases coexist, differ only by $\sim$0.05 eV.

Traditionally, the T dependence of band gap is thought to be a result of two contributions, the lattice expansion ($E_{g,lat.}$) and the atomic displacements (or electron–phonon interaction, $E_{g,at.}$).[67] Our approach allows us to separate these two terms. To identify the $E_{g,lat.}$ term, the band gap is computed for a set of relaxed structures with cell geometries set to those predicted (as ensemble averages) by the *NPT* MD simulations presented in Section 3.2. Since the relaxation procedure ensures that the net forces acting on each atom vanish, the atoms in these relaxed structures sit in their optimal unperturbed positions. Consequently, the band gap dependence on volume includes the cell expansion contribution only, while the atomic displacement contribution vanishes. The latter dependence is therefore identified as $E_{g,lat.}(V) = E_g(V)$. Because the ensemble averaged cell geometry is fixed by temperature, the T-dependence of the

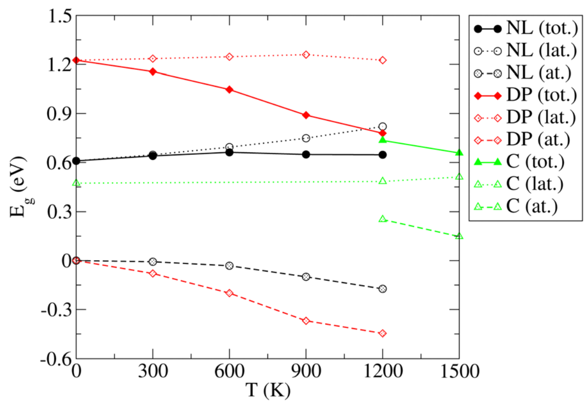

Fig. 6 Variation of the band gap (E_g) of the NL, DP, and C phases of $SrZrS_3$ with temperature. Lattice (lat.) and atomic displacement (at.) contributions to the total (tot.) values are shown.

$E_{g,lat.}$ term is obtained as $E_{g,lat.}(T) = E_{g,lat.}(V(T))$. Finally, the atomic displacement contribution is determined trivially *via* $E_{g,at.} = E_g - E_{g,lat.}$. As shown in Fig. 6, the lattice contribution is always positive but differs in magnitude for different phases. For NL, $E_{g,lat.}$ increases monotoneously with T and ranges between 0.61 eV (0 K) and 0.82 eV (1200 K). In contrast, $E_{g,lat.}$ determined for the DP and C phases, is nearly constant over the entire T range considered here (variations within 0.04 eV). The atomic displacement contributions for the NL and DP phases are negative and decrease monotoneously with T (by up to −0.17 eV (NL) and −0.45 eV (DP) at 1200 K). In the C phase, $E_{g,at.}$ becomes positive and decreases with T such that at 1500 K, where the C phase is fully formed, the atomic displacement contribution to the band gap is only 0.15 eV.

To demonstrate that the very large atomic displacement contribution to the band gap of DP phase is indeed a consequence of proximity to the parent C phase, we computed E_g values for a series of structures created by interpolation of relaxed C and DP structures as follows:

$$q_X = q_0 + X(q_1 - q_0), \quad (3)$$

where X is a distortion parameter ranging from 0 (relaxed C) to 1 (relaxed DP) and q_X represents the atomic and lattice coordinates of the structure corresponding to X. As shown in Fig. 7, the band gap of a structure created by symmetry breaking of the cubic phase can indeed be continuously varied from the value characteristic for the relaxed C to that of relaxed DP *via* change of X. As discussed in Section 3.2, such a quasi-continuous transition from DP to C occurs at a finite temperature, whereby X naturally changes as a result of thermal motion of atoms (see Fig. 4 and 5). All finite T values of the band gap of DP/C structures calculated here therefore fall into the interval delimited by the E_g of the relaxed C and DP. We note that the proximity of two phases – tetragonal and cubic – was found in previous *NVT* MD simulations of Quarti *et al.*[21] to affect also the T dependence of E_g of another perovskite material $CH_3NH_3PbI_3$, albeit the extent of this effect was much smaller (blueshift by ∼0.05 eV upon increasing T from 320 K to 650 K).

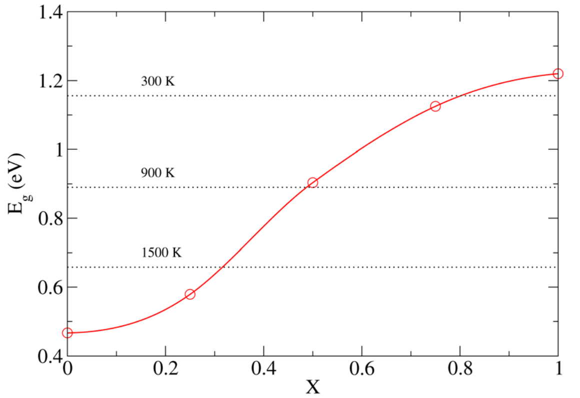

Fig. 7 Zero temperature band gap (E_g) variation with distortion (X) of a cubic structure defined so that X = 0 and X = 1 correspond to relaxed C and DP phases, respectively. Horizontal dotted lines show the finite-T values of E_g as obtained from molecular dynamics.

As already discussed in Section 3.1, the PBE functional used throughout this work strongly underestimates the values of E_g for the NL and DP phases. Therefore, it is important to confirm that the conclusions regarding the dependence of E_g on temperature discussed above are correct. In particular, we wish to test if the predicted trends remain the same upon replacing the PBE functional by the HSE06 method, which is known to yield accurate predictions for the chalcogenide perovskite compounds[23] and which significantly improves the E_g predictions in static calculations (see Section 3.1). Unfortunately, the HSE06 calculations are about 80-times more time-consuming than those performed at the PBE level, rendering the recalculation of E_g for all configurations, used to draw ensemble averages in our finite T simulations, impractical. We note, however, that the HSE06 and PBE values of E_g are strongly linearly correlated (see Fig. S14–S16 (ESI†)). We therefore devised an efficient computational scheme, in which we performed only 20–40 explicit E_g calculations at the HSE06 level for each temperature. We then set up a linear regression model and used it to predict the HSE06 E_g values for all 200 configurations used in the PBE calculations to determine the ensemble average. The calculated HSE06 and PBE ensemble averages of E_g are compared in Fig. 8 (the corresponding numerical values are presented in Table S5 (ESI†)). As expected, the HSE06 band gaps are larger by 0.5–0.8 eV compared to the PBE counterparts. Importantly, however, both methods predict very similar overall trends. We conclude therefore that although the PBE underestimates the absolute values of the band gaps systematically, it is still quite reliable in predicting the thermal dependence of E_g. Finally, comparing the band gaps obtained at the HSE06 level for 0 K (1.40 (NL), 2.04 (DP)) and 300 K (1.36 eV (NL), 1.96 eV (DP)) with the experiment conducted at ambient conditions (1.53 eV (NL), 2.05-2.13 eV (DP)),[15] we observe that the systematic error of the HSE06 functional is ∼0.1 eV when thermal effects are taken into account and hence the agreement with the experiment remains reasonably good. As discussed in the literature,[23] further improvements can be achieved by inclusion of relativistic spin–orbit coupling effects and improved treatment of many-body electronic problem (*e.g.*, *via* Green's function

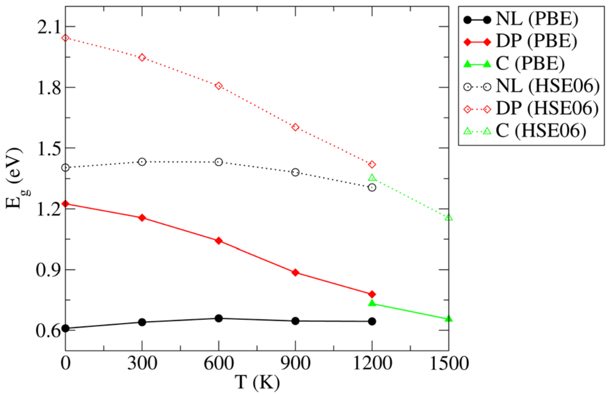

Fig. 8 Comparison of the PBE and HSE06 predictions of the variation of electronic band gap (E_g) of the needle-like (NL), distorted perovskite (DP), and cubic (C) phases of $SrZrS_3$ with temperature.

(GW) methods). This is, however, beyond the scope of the present work.

4 Conclusions

Ab initio based molecular dynamics simulations in an *NPT* ensemble were performed to investigate properties of the NL and DP phases of $SrZrS_3$ in the temperature range between 300 K and 1200 K. Compared to a straightforward ab intio MD, the use of the adaptive machine learning scheme implemented[35,36] in VASP allowed us to extend the simulation times from few tens of picoseconds to nanoseconds improving thus the sampling quality greatly. The structural changes occurring in the NL phase upon heating are relatively modest and include an anisotropic but monotonous lattice expansion. The changes are much more dramatic in the DP phase, as the evolution of both the lattice geometry and the internal structure is strongly affected by the proximity of the cubic phase. Although the temperature induced process of conversion of DP to C is seemingly continuous, abrupt changes in the lattice parameters were detected at 1200 K, when both phases co-exist. The transition is complete at 1500 K.

The isothermal bulk modulus, computed from the cell volume fluctuations, was found to decrease linearly with T, with the slope of 0.014 GPa K^{-1} and 0.020 GPa K^{-1} for NL and DP, respectively.

The finite temperature effect on the band gap of $SrZrS_3$ was investigated. Since we determined E_g as an observable in *NPT* MD, our approach describes both the lattice expansion and atomic displacement (electron–phonon coupling) contributions to the thermal dependence of the band gap. The calculated PBE band gaps for the NL phase were found to be virtually temperature independent in the 300–1200 K range. In contrast, the E_g of the DP phase was found to decrease monotonously with T, whereby the value obtained for 1200 K is 0.45 eV lower than that obtained for 300 K. The analysis revealed that the observed E_g decrease is almost exclusively due to the large atomic displacements which are, in turn, a consequence of the proximity of the DP phase to the parent C phase, with the band gap lower by $\sim$0.8 eV. The important observation is that the temperature causes a gradual conversion of the DP phase into the C phase which is linked to the E_g reduction. Our results show that this process starts well below the temperatures at which the C phase becomes stable (see Fig. 8). The results obtained by the PBE simulations were validated by additional calculations using the HSE06 functional, which yields band gap values that are in a much better agreement with the experiment. Since the E_g *vs.* T trends obtained by the two methods are nearly identical, it is concluded that the use of a less CPU intense PBE functional is justified in the future finite-T analysis of the electronic structure in materials similar to $SrZrS_3$.

To be suitable for application in photovoltaics, the material electronic band gap should fall within the range of 0.9–1.6 eV.[68] In case of $SrZrS_3$ the calculated band gap for NL is about 1.4 eV,[23] which is within the desired range. However, according to Sun *et al.*,[23] the onset of the optical absorption in NL phase is significantly higher than its band gap and therefore this phase of the material is not suitable for application in photovoltaics. Our results show that the NL phase exhibits a very modest dependence of its structure and band gap on temperature. On the other hand, the band gap of DP phase of the $SrZrS_3$ was theoretically predicted to be about 2.0 eV,[23] *i.e.*, above the optimal photovoltaic range. However, our study reveals that, thanks to the interesting dynamic response being a consequence of proximity to the cubic phase, the band gap of this phase moves closer to the optimum range with increasing temperature. Since the phase transition from the DP to cubic is quite steady and progressive, the decrease in the band gap is significant, but not abrupt. We anticipate that in closer inspection similar behavior will be observed in for other TCs provided that: (i) there is a significant difference between the band gaps of DP and C phase and (ii) the C phase is less stable than the DP phase, but still energetically accessible. Our exploratory static results suggest that number of sulfides and selenides meet these requirements (see Fig. S17 and Table S6 (ESI†)). Moreover, judging from smaller energy differences between the DP and C phases found for some compounds, some of the TCs are likely to transform to the cubic phase at much lower temperatures than the DP phase of the $SrZrS_3$, with the effect on the band gap being even more dramatic. These deeper insights into the structure-band gap relationship in TCs are essential for identifying the materials with the optimal properties for photovoltaics and other applications. We hope this work will stimulate further studies in this direction.

Author contributions

Namrata Jaykhedkar: investigation, visualization, writing-original draft preparation. Roman Bystrický: investigation, writing-reviewing and editing. Milan Sýkora: conceptualization, funding acquisition, project administration, writing-reviewing and editing. Tomáš Bučko: conceptualization, investigation, formal analysis, visualization, writing-original draft preparation.

Conflicts of interest

There are no conflicts to declare.

Acknowledgements

This work was supported by the European Union's Horizon 2020 research and innovation programme under grant agreement No. 810701 and by the Slovak Research and Development Agency under grant agreement No. APVV-19-0410. NJ and TB gratefully acknowledge the use of HPC facility by PRACE (Partnership for Advanced Computing in Europe) within the programme DECI-16 and of the supercomputing infrastructure of Computing Center of the Slovak Academy of Sciences acquired in projects ITMS 26230120002 and 26210120002 supported by the Research and Development Operational Program funded by the ERDF. The use of the high performance computing facilities CLARA@UNIBA.SK at Comenius University in Bratislava, services and staff expertise of Centre for Information Technology is acknowledged. TB is thankful to Dr Ryosuke Jinnouchi and Dr Ferenc Karsai for introducing him the MLFF method.

References

1 J. Berry, T. Buonassisi, D. A. Egger, G. Hodes, L. Kronik, Y.-L. Loo, I. Lubomirsky, S. R. Marder, Y. Mastai, J. S. Miller, D. B. Mitzi, Y. Paz, A. M. Rappe, I. Riess, B. Rybtchinski, O. Stafsudd, V. Stevanovic, M. F. Toney, D. Zitoun, A. Kahn, D. Ginley and D. Cahen, *Adv. Mater.*, 2015, **27**, 5102–5112.

2 D. A. Egger, A. M. Rappe and L. Kronik, *Acc. Chem. Res.*, 2016, **49**, 573–581.

3 H. J. Snaith, *Nat. Mater.*, 2018, **17**, 372–376.

4 S.-T. Ha, R. Su, J. Xing, Q. Zhang and Q. Xiong, *Chem. Sci.*, 2017, **8**, 2522–2536.

5 N.-G. Park, *J. Phys. Chem. Lett.*, 2013, **4**, 2423–2429.

6 F. Chiarella, A. Zappettini, F. Licci, I. Borriello, G. Cantele, D. Ninno, A. Cassinese and R. Vaglio, *Phys. Rev. B*, 2008, **77**, 045129.

7 B. Kshirsagar, N. Jaykhedkar, K. Jain, S. Kishor, V. Shah, L. M. Ramaniah and S. Tiwari, *J. Phys. Chem. C*, 2021, **125**, 2592–2606.

8 D. B. Straus, S. Guo, A. M. Abeykoon and R. J. Cava, *J. Adv. Mater.*, 2020, **32**, 2001069.

9 T. Gupta, D. Ghoshal, A. Yoshimura, S. Basu, P. K. Chow, A. S. Lakhnot, J. Pandey, J. M. Warrender, H. Efstathiadis, A. Soni, E. Osei-Agyemang, G. Balasubramanian, S. Zhang, S.-F. Shi, T.-M. Lu, V. Meunier and N. Koratkar, *Adv. Funct. Mater.*, 2020, **30**, 2001387.

10 K. V. Sopiha, C. Comparotto, J. A. Márquez and J. J. S. Scragg, *Adv. Opt. Mater.*, 2021, 2101704.

11 D. Tiwari, O. S. Hutter and G. Longo, *J. Phys. Energy*, 2021, **3**, 034010.

12 A. Swarnkar, W. J. Mir, R. Chakraborty, M. Jagadeeswararao, T. Sheikh and A. Nag, *Chem. Mater.*, 2019, **31**, 565–575.

13 C.-S. Lee, K. Kleinke and H. Kleinke, *Solid State Sci.*, 2005, **7**, 1049–1054.

14 S. Perera, H. Hui, C. Zhao, H. Xue, F. Sun, C. Deng, N. Gross, C. Milleville, X. Xu, D. F. Watson, B. Weinstein, Y.-Y. Sun, S. Zhang and H. Zeng, *Nano Energy*, 2016, **22**, 129–135.

15 S. Niu, H. Huyan, Y. Liu, M. Yeung, K. Ye, L. Blankemeier, T. Orvis, D. Sarkar, D. J. Singh, R. Kapadia and J. Ravichandran, *Adv. Mater.*, 2017, **29**, 1604733.

16 S. Niu, J. Milam-Guerrero, Y. Zhou, K. Ye, B. Zhao, B. C. Melot and J. Ravichandran, *J. Mater. Res.*, 2018, **33**, 4135–4143.

17 N. Gross, Y.-Y. Sun, S. Perera, H. Hui, X. Wei, S. Zhang, H. Zeng and B. A. Weinstein, *Phys. Rev. Appl.*, 2017, **8**, 044014.

18 M. Oumertem, D. Maouche, S. Berri, N. Bouarissa, D. P. Rai, R. Khenata and M. Ibrir, *J. Comput. Electron.*, 2019, **18**, 415–427.

19 A. Majumdar, A. A. Adeleke, S. Chakraborty and R. Ahuja, *J. Mater. Chem. C*, 2020, **8**, 16392–16403.

20 G. Mannino, I. Deretzis, E. Smecca, A. La Magna, A. Alberti, D. Ceratti and D. Cahen, *J. Phys. Chem. Lett.*, 2020, **11**, 2490–2496.

21 C. Quarti, E. Mosconi, J. M. Ball, V. D'Innocenzo, C. Tao, S. Pathak, H. J. Snaith, A. Petrozza and F. De Angelis, *Energy Environ. Sci.*, 2016, **9**, 155–163.

22 Y.-N. Wu, W. A. Saidi, J. K. Wuenschell, T. Tadano, P. Ohodnicki, B. Chorpening and Y. Duan, *J. Phys. Chem. Lett.*, 2020, **11**, 2518–2523.

23 Y.-Y. Sun, M. L. Agiorgousis, P. Zhang and S. Zhang, *Nano Lett.*, 2015, **15**, 581–585.

24 A. Clearfield, *Acta Crystallogr.*, 1963, **16**, 135–142.

25 R. Lelieveld and D. J. W. IJdo, *Acta. Crystallogr. B.*, 1980, **36**, 2223–2226.

26 H. Igwebuike, E. Ntsoenzok and N. Dzade, *Materials*, 2020, **13**, 978.

27 Y. Nishigaki, T. Nagai, M. Nishiwaki, T. Aizawa, M. Kozawa, K. Hanzawa, Y. Kato, H. Sai, H. Hiramatsu, H. Hosono and H. Fujiwara, *Sol. RRL*, 2020, **4**, 1900555.

28 P. B. Allen and V. Heine, *J. Phys. C: Solid State Phys.*, 1976, **9**, 2305–2312.

29 P. B. Allen and M. Cardona, *Phys. Rev. B*, 1981, **23**, 1495–1505.

30 J. Park, W. Saidi, J. Wuenschell, B. Howard, B. Chorpening and Y. Duan, *ACS Appl. Mater. Interfaces*, 2021, **13**(15), 17717–17725.

31 W. A. Saidi, S. Poncé and B. Monserrat, *J. Phys. Chem. Lett.*, 2016, **7**, 5247–5252.

32 M. Zacharias and F. Giustino, *Phys. Rev. B*, 2016, **94**, 075125.

33 F. Karsai, M. Engel, E. Flage-Larsen and G. Kresse, *New J. Phys.*, 2018, **20**, 123008.

34 S. Baroni, P. Giannozzi and E. Isaev, in *Density-Functional Perturbation Theory for Quasi-Harmonic Calculations*, ed. R. Wentzcovitch and L. Stixrude, 2010, vol. 71, pp. 39–57.

35 R. Jinnouchi, F. Karsai and G. Kresse, *Phys. Rev. B*, 2019, **100**, 014105.

36 R. Jinnouchi, F. Karsai, C. Verdi, R. Asahi and G. Kresse, *J. Chem. Phys.*, 2020, **152**, 234102.

37 P. Liu, C. Verdi, F. Karsai and G. Kresse, *Phys. Rev. B*, 2022, **105**, L060102.

38 C. Verdi, F. Karsai, P. Liu, R. Jinnouchi and G. Kresse, *npj Comput. Mater.*, 2021, **7**, 156.

39 R. Jinnouchi, F. Karsai, C. Verdi and G. Kresse, *J. Chem. Phys.*, 2021, **154**, 094107.

40 R. Jinnouchi, J. Lahnsteiner, F. Karsai, G. Kresse and M. Bokdam, *Phys. Rev. Lett.*, 2019, **122**, 225701.

41 P. Blöchl, *Phys. Rev. B*, 1994, **50**, 17953.

42 G. Kresse and D. Joubert, *Phys. Rev. B*, 1999, **59**, 1758–1775.

43 J. P. Perdew, K. Burke and M. Ernzerhof, *Phys. Rev. Lett.*, 1996, **77**, 3865–3868.

44 T. Bucko, J. Hafner and J. G. Angyan, *J. Chem. Phys.*, 2005, **122**, 124508.

45 M. Parrinello and A. Rahman, *Phys. Rev. Lett.*, 1980, **45**, 1196–1199.

46 M. Parrinello and A. Rahman, *J. Appl. Phys.*, 1981, **52**, 7182–7190.

47 D. Frenkel and B. Smit, *Understanding molecular simulation: From algorithms to applications*, Academic Press, San Diego, 2002, pp. 74–77.

48 J. Behler and M. Parrinello, *Phys. Rev. Lett.*, 2007, **98**, 146401.
49 C. M. Bishop, *Pattern Recognition and Machine Learning*, Springer, 2006.
50 S. K. Schiferl and D. C. Wallace, *J. Chem. Phys.*, 1985, **83**, 5203–5209.
51 H. Flyvbjerg and H. Petersen, *J. Chem. Phys.*, 1989, **91**, 461–466.
52 K. Momma and F. Izumi, *J. Appl. Crystallogr.*, 2011, **44**, 1272–1276.
53 F. D. Murnaghan, *P. Natl. Acad. Sci. U. S. A.*, 1944, **30**, 244–247.
54 J. F. Dobson, K. McLennan, A. Rubio, J. Wang, T. Gould, H. M. Le and B. P. Dinte, *Aust. J. Chem.*, 2001, **54**, 513–527.
55 S. Grimme, *J. Comput. Chem.*, 2006, **27**, 1787–1799.
56 A. Tkatchenko and M. Scheffler, *Phys. Rev. Lett.*, 2009, **102**, 073005.
57 S. Grimme, J. Antony, S. Ehrlich and H. Krieg, *J. Chem. Phys.*, 2010, **132**, 154104.
58 T. Bučko, S. Lebègue, J. Hafner and J. Ángyán, *J. Chem. Theory Comput.*, 2013, **9**, 4293–4299.
59 T. Bučko, S. Lebègue, J. G. Ángyán and J. Hafner, *J. Chem. Phys.*, 2014, **141**, 034114.
60 A. Ambrosetti, A. M. Reilly, R. A. DiStasio and A. Tkatchenko, *J. Chem. Phys.*, 2014, **140**, 18A508.
61 T. Gould, S. Lebègue, J. G. Ángyán and T. Bučko, *J. Chem. Theory Comput.*, 2016, **12**, 5920–5930.
62 N. W. Ashcroft and N. D. Mermin, *Solid State Physics*, Harcourt College Publisher, 1976, pp. 151–174.
63 C. Kittel, *Introduction to Solid State Physics*, Wiley, 2004, pp. 223–254.
64 J. Heyd, G. E. Scuseria and M. Ernzerhof, *J. Chem. Phys.*, 2003, **118**, 8207–8215.
65 J. Heyd, G. E. Scuseria and M. Ernzerhof, *J. Chem. Phys.*, 2006, **124**, 219906.
66 J. Paier, R. Hirschl, M. Marsman and G. Kresse, *J. Chem. Phys.*, 2005, **122**, 234102.
67 Y. Varshni, *Physica*, 1967, **34**, 149–154.
68 M.-G. Ju, J. Dai, L. Ma and X. C. Zeng, *Adv. Energy Mater.*, 2017, **7**, 1700216.